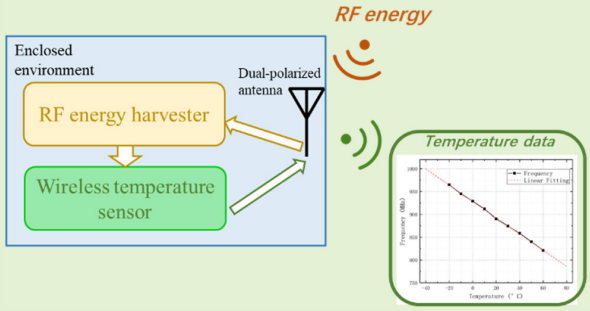
# Wireless Sensing System Powered by RF Energy for Temperature Monitoring With 7.9-mK Resolution

Zihan Yu, Changrong Liu, *Member, IEEE*, Baoqing Nie, and Dacheng Xu

***Abstract*—This article proposes a wireless temperature sensing system powered by RF energy for high-accuracy temperature monitoring. To enable wireless temperature sensing, the RF energy harvester and frequency-based temperature sensors have been designed. The temperature sensor generates a signal whose frequency is linearly related to temperature. The RF energy harvester harvests RF energy to power the sensor without a battery. A dual-polarized antenna is designed to simultaneously transfer RF energy and temperature data. It features a bandwidth of 0.665–1.295 GHz and a peak gain of ∼7 dBi. Experimental results demonstrate that the system achieves a temperature resolution of ∼7.9 mK in the temperature range from −35 °C to 80 °C, a communication distance of 10 m, an average power consumption of 1.68 mW at a distance of 2 m and 12.4 $\mu$W at a distance of 10 m, and a minimum operating power of −10 dBm. The performance of the proposed system indicates its potential for wireless high-precision temperature sensing applications.**




***Index Terms*— Dual-polarization, radio frequency energy harvest, self-powered sensor node, wireless temperature sensor.**

## I. Introduction

TEMPERATURE is one of the most frequently measured physical quantities, playing a crucial role in industrial [1], meteorological [2], and medical [3] applications. Within the industrial sector, abnormal temperature fluctuations are often closely correlated with equipment failures. Temperature monitoring is therefore critically important for the timely detection of equipment failures and the prevention of severe accidents such as fires [4].

Enclosed environments, such as pipelines and containers, are often present in industrial and electrical equipment. In such scenarios, wired measurement methods face difficulty in penetrating the shells of pipelines and containers [5]. Battery-powered wireless temperature measurement approaches face challenges associated with battery replacement. Replacing batteries typically requires draining the containers, which increases the maintenance cost. For pipelines, it is nearly impossible for personnel to get inside to replace batteries. To address the limitations of these conventional temperature measurement methods, wireless battery-free temperature sensors have demonstrated increasingly significant application potential [6]. Battery-free wireless temperature sensors can be categorized into two types based on their operational principle: passive and self-powered. Passive wireless temperature sensors sense temperature through the parameter variations of their passive components, and couple with an external detector via a coil or an antenna. For instance, in [7], a temperature-sensitive capacitor combined with a coil was utilized to form an *LC* resonator, whose resonant frequency shifts with temperature. Dong et al. [8] used the intrinsic temperature-dependent characteristics of the antenna itself for temperature sensing. Passive temperature sensors are unaffected by the operating temperature limitations of integrated circuits, thereby enabling an exceptionally wide measurement range [9]. However, since these sensors cannot actively transmit signals, they generally lack long communication distances. For example, *LC* resonant sensors typically exhibit communication ranges limited to several tens of centimeters.

Wireless-powered temperature sensors rely on energy harvesting techniques for operation instead of batteries [10]. Industrial environments offer inherent energy sources for such sensors, including high-power, high-temperature, and rotating equipment. Consequently, various energy harvesting

Received 15 October 2025; accepted 12 November 2025. Date of publication 25 November 2025; date of current version 30 December 2025. This work was supported in part by the National Key Research and Development Program of China under Grant 2023YFB3207903. The associate editor coordinating the review of this article and approving it for publication was Prof. Jean-Michel Redoute. *(Corresponding author: Changrong Liu.)*

The authors are with the School of Electronic and Information Engineering, Soochow University, Suzhou, Jiangsu 215006, China (e-mail: crliu@suda.edu.cn).

Digital Object Identifier 10.1109/JSEN.2025.3634544

1558-1748 © 2025 IEEE. All rights reserved, including rights for text and data mining, and training of artificial intelligence and similar technologies. Personal use is permitted, but republication/redistribution requires IEEE permission.
See https://www.ieee.org/publications/rights/index.html for more information.
Authorized licensed use limited to: Soochow University. Downloaded on October 13,2026 at 13:10:41 UTC from IEEE Xplore. Restrictions apply.

methods have been developed specifically for these application scenarios. For instance, targeting high-power equipment, electromagnetic coupling was proposed to harvest energy from power cables [11], [12]. Magnetically excited cantilever beams are another way to extract energy from the magnetic field generated by power cables, and then, the vibration energy is converted to electrical energy by a piezoelectric plate [13], [14], [15], [16]. For high-temperature equipment, thermoelectric generation (TEG) is preferred to power the sensors [17], [18], [19], [20]. A limitation of the abovementioned energy harvesting devices is that they are required to be placed near the cables or equipment. For operation in other locations, radio frequency energy harvesting (RFEH) stands out for its flexibility, resistance to environmental change, and low cost [21], [22], [23], [24], [25].

RFEH-based wireless-powered sensors harvest radio frequency energy and transmit data through their antennas. The most common architecture employs two separate antennas dedicated to energy harvesting and data transmission. This approach, however, increases system volume and complexity. While some of the RFEH works apply dual-polarized antennas, aiming to harvest energy from multiple bands. In [26], a dual-polarized antenna was utilized to harvest ambient RF energy and receive wireless energy from a dedicated source simultaneously. In [27], a dual-polarized antenna was implemented to harvest RF energy from both horizontal and vertical polarizations. In this article, the proposed wireless sensing system has a new type of architecture where a dual-polarized antenna was applied to transfer RF energy and data simultaneously. This approach reduces the number of antennas and thus improves integrity and bulk.

This study proposed a wireless-powered temperature sensing system designed for monitoring complex and harsh environmental temperatures. This system consists of a temperature sensor and an RF energy harvester. The output frequency of the system exhibits linear variation with temperature, thereby enabling temperature sensing. The system is battery-less and can be powered by RF energy. It operates with a minimum input power of $-10$ dBm. A high-gain wideband dual-polarized antenna was proposed to enable the simultaneous transmission of RF energy and temperature data.

Among the state-of-the-art wireless energy-harvest-based temperature sensors, this work has a high-temperature resolution (7.9 mK) enabled by frequency-based temperature sensing architecture, and an extended operating range (10 m) among the state-of-the-art RFEH-based sensing systems.

The rest of this article is structured as follows. Section II describes the overall architecture of the system and the design of each circuit module. In Section III, experiments were carried out to test the performance of the modules in the system individually. In Section IV, all modules were assembled to test the performance of the complete wireless temperature sensing system, and Section V summarizes this work.

## II. Circuit Design

### A. System Architecture

Fig. 1 presents the block diagram of the circuit structure of this work. The wireless self-powered temperature sensing system consists of two parts: a temperature sensor and an energy harvester. The temperature sensor consists of a temperature-to-frequency converter (TFC) and a phase-locked loop (PLL). The TFC generates a low-frequency signal whose frequency is correlated with the temperature. The output signal of TFC is then multiplied by the PLL to the 915-MHz ultrahigh-frequency (UHF) band for wireless transmission. $\Delta f$ caused by the temperature change can be increased by the PLL circuit, thus increasing the temperature accuracy.

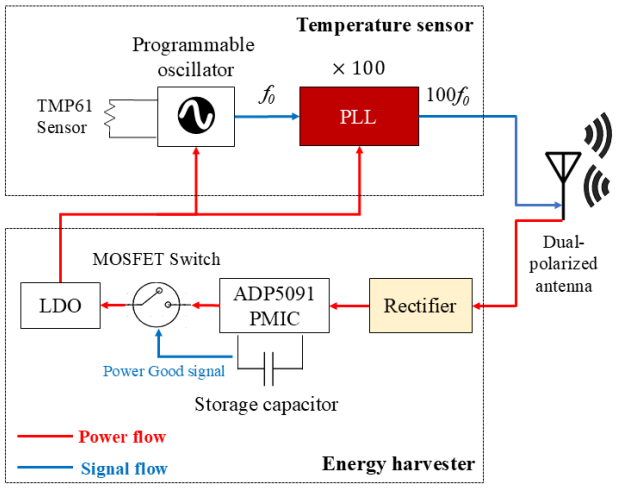



Fig. 1. Block diagram of the wireless sensing system.

The second part is the RF energy harvester, which consists of an RF rectifier and a power management system. The RF rectifier converts the RF energy into direct current (dc) energy. The power management system stores the dc energy in a capacitor and manages the charging and discharging process of the capacitor.

Besides, a $\pm 45°$ dual-polarized antenna with high isolation is utilized for the reception of the RF energy and transmission of the temperature data. The dual-polarized antenna has two orthogonal polarization directions, in which both energy and temperature data can be received and transmitted independently.

### B. Design of the TFC

The TFC consists of a programmable oscillator (LTC6908, Linear Technology) and a PTC thermistor (TMP61, Texas Instruments). The output frequency of the programmable oscillator is configured by an external resistor so that temperature sensing is enabled by combining the programmable oscillator with the PTC resistor. Additional cascade and shunt resistors are utilized to make the output frequency of the TFC range from 7.7 to 9.9 MHz, which matches the output frequency of the PLL.

### C. Design of a PLL

PLL is used to multiply the output signal of the TFC to operate at the UHF band. Also, the PLL circuit is a feedback system, in which a voltage-controlled oscillator (VCO) and a frequency-discriminating phase-discriminator (PFD) form

Authorized licensed use limited to: Soochow University. Downloaded on October 13,2026 at 13:10:41 UTC from IEEE Xplore. Restrictions apply.

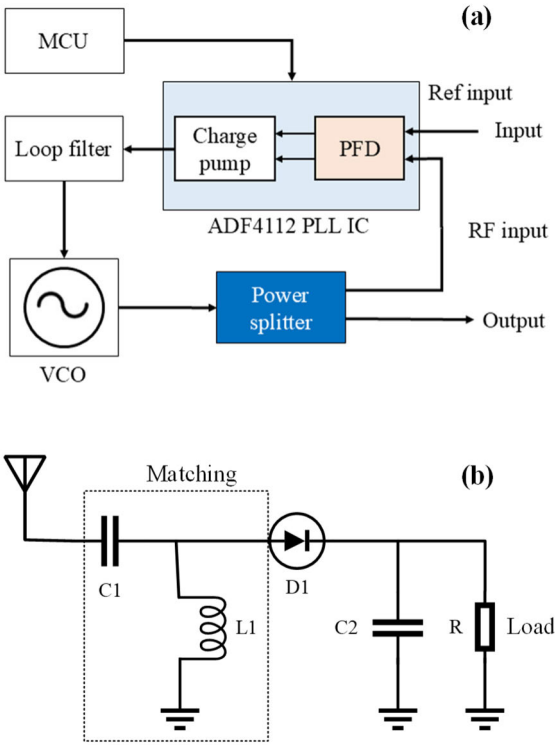



Fig. 2. (a) Block diagram of the PLL. (b) Schematic of the rectifier.

a feedback loop that can be used to generate low-noise, high-frequency signals from low-frequency signals. A complete PLL also includes a charge pump (CP), a loop filter, and an N-divider. The feedback loop forces the two input signals of the PFD to be in phase, so the frequency of the output signal is equal to the input signal frequency multiplied by the value of the N-divider.

To extend the transmitting time and reduce charging time, this system adopts the low power consumption PLL and VCO combination. PLL adopts ADF4112 (Analog Devices), VCO adopts MAX2622 (MAXIM), and the power consumption of the PLL part of the system is as low as 13 mA. The circuit diagram of the PLL part is shown in Fig. 2(a). ADF4112 integrates the PFD, CP, and N-divider parts of the PLL. The output signal of the CP is filtered by the external loop filter with a loop bandwidth of 10 kHz to control the output frequency of the VCO. The power splitter divides the output signal of the VCO into two parts. One part is fed back to the ADF4112, forming a complete feedback loop, and the other part is transmitted through the antenna.

A microcontroller unit (MCU) is used to enable and initialize the PLL at power-up, and then, it enters standby mode once the initialization is complete to reduce the power consumption.

### D. Design of a Rectifier Circuit

The rectifier comprises a matching network, a diode, and a load. As illustrated in Fig. 2(b), the matching network serves to properly match the input signal of a specific frequency to the subsequent rectifying circuit while preventing higher order harmonics generated by the rectifier from backpropagating through the antenna [10]. The diode and capacitor form a half-bridge rectifier circuit, which converts the alternating current (ac) signal into a dc signal.

The values of the components and the layout were designed and optimized in advanced design system (ADS). The detailed parameters of the layout are listed in Table I.

TABLE I
DETAILED PARAMETERS OF THE RECTIFIER

| Symbol | Value | Symbol | Value |
|---|---|---|---|
| *C1* | 1pF | L1 | 10nH |
| C2 | 10nF | D1 | HSMS-2850 |

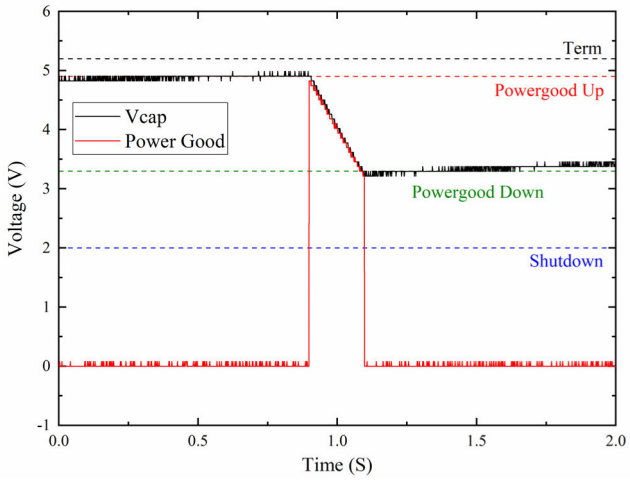



Fig. 3. Charging process of the power management system.

### E. Design of a Power Management System

The power management system manages the charge and discharge process of the capacitor and provides a stable dc voltage for the sensor part. It employs the ADP5091 (Analog Devices) power management integrated circuit, which integrates a BOOST step-up converter, a maximum power point tracking (MPPT) controller, and a power routing management circuitry. The MPPT controller maintains the rectifier at its peak efficiency operating point by adjusting the duty cycle. The BOOST circuit upconverts the dc voltage from the rectifier to charge the supercapacitor (denoted as storage capacitor in Fig. 1). Fig. 3 illustrates the charging and discharging process of the power management system, where the charging and discharging processes are governed by four voltage thresholds: shutdown ($V_{SD}$), termination ($V_{TERM}$), power good (PG) rising ($V_{UP}$), and PG falling ($V_{FALL}$).

As charging progresses, the capacitor voltage increases. When reaching $V_{UP}$, the PG pin activates an external MOSFET switch, and then, the capacitor starts to discharge, enabling sensor operation. When the capacitor voltage drops to $V_{FALL}$, the PG pin deactivates the MOSFET switch to halt sensor operation, and the capacitor starts to recharge. The $V_{TERM}$ threshold prevents overcharging. When the capacitor voltage exceeds $V_{TERM}$, the BOOST circuit ceases operation. The $V_{SD}$ threshold prevents overdischarging. Below $V_{SD}$, the capacitor's output path is disabled. Consequently, the total energy

Authorized licensed use limited to: Soochow University. Downloaded on October 13,2026 at 13:10:41 UTC from IEEE Xplore. Restrictions apply.

delivered per complete discharge cycle (from $V_{UP}$ to $V_{FALL}$) is given by

$$E_{cap} = \frac{C}{2}\left(V_{UP}^2 - V_{FALL}^2\right) \tag{1}$$

where $E$ represents the output energy and $C$ represents the capacitance.

The output voltage from the energy harvesting circuit is stepped down to 3.3 V via a low-dropout (LDO) regulator to power the sensor part. Given that the LDO's output current approximates its input current, the duration of a single discharge cycle is

$$\tau_{on} = \frac{C\,(V_{UP} - V_{FALL})}{I} \tag{2}$$

where $I$ refers to the operating current of the sensing circuitry. Also, the overall efficiency of LDO equals

$$\eta_{LDO} = \frac{V_{out} I \tau_{on}}{E} = \frac{2V_{out}}{V_{UP} + V_{FALL}} \tag{3}$$

where $V_{out}$ refers to the output voltage of the LDO. Equations (2) and (3) show a tradeoff between transmitting time and LDO efficiency. Increasing the voltage differential between charge and discharge thresholds extends discharge time, enhancing temperature measurement precision at the cost of prolonged charging duration and reduced overall efficiency. Conversely, reducing this differential shortens charging time, thereby improving data update rate.

The signals measured by an oscilloscope (Keysight DSOX2002A) on the capacitor ($V_{cap}$) and the PG pin are shown in Fig. 3, showing a $V_{UP}$ voltage of 4.9 V and a $V_{FALL}$ voltage of 3.3 V. The discharging duration of the sensing system is thus set as 200 ms for testing based on the spectrum analyzer used in this study. Note that, the discharge duration depends on the response time of the entire wireless temperature measurement system.

### F. Dual-Polarized Antenna

The performance of the antenna plays a critical role in the overall functionality of the sensing system. To extend the operational range of the system, the antenna gain should be as high as possible, thereby enhancing the amount of RF energy harvested by the RF energy harvester from the reader. Given that the output frequency of the temperature sensor ranges from 770 to 990 MHz, and the RF energy harvester operates in the 997-MHz band, the antenna bandwidth must cover the frequency range from 770 to 997 MHz. Driven by the operational requirements of the proposed sensing system in this article, a high-gain, wideband dual-polarized antenna is designed.

To power the temperature sensor and receive the temperature data wirelessly, a ±45° dual-polarized antenna was proposed, as can be seen in Fig. 4. The detailed dimensions are listed in Table II.

The antenna was designed on a two-layer FR4 substrate with a thickness of 0.8 mm. The radius of the substrate is 75 mm. The distance between the ground and the substrate is 90 mm.

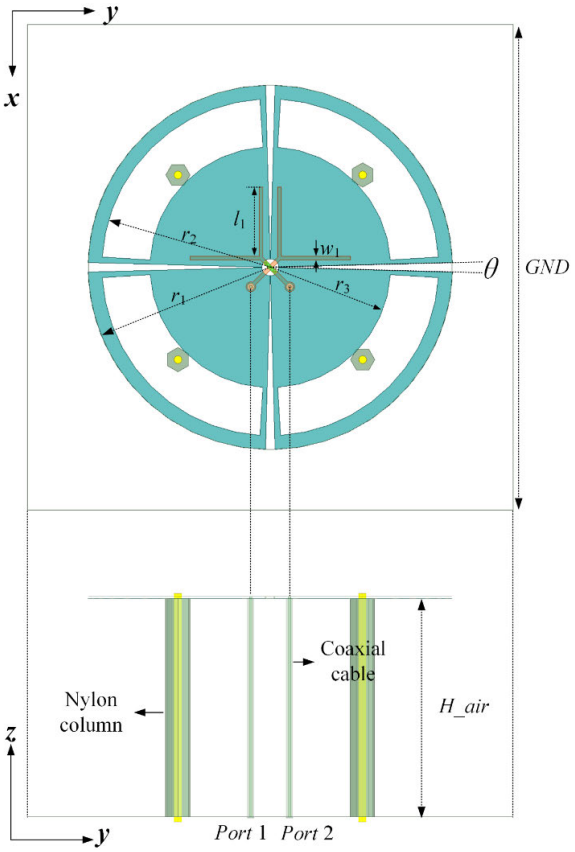



Fig. 4. Structure of the dual-polarized antenna.

TABLE II
DETAILED DIMENSIONS OF THE DUAL-POLARIZED ANTENNA IN MILLIMETERS

| Symbol | Value | Symbol | Value |
|---|---|---|---|
| $r_1$ | 75 | $w_1$ | 1.5 |
| $r_2$ | 70 | $H_air$ | 90 |
| $r_3$ | 49 | $\theta$ | 3 |
| $l_1$ | 30 | $GND$ | 200 |

## III. MANUFACTURING AND TESTING

### A. Structure and Layout

Fig. 5 depicts the photograph of the fabricated sensing. As can be seen, the sensing system consists of a circuit board and a dual-polarized antenna, and the circuit is a four-layer FR4 board with 1.6 mm in thickness and 20 × 20 cm in size, and the dual-polarized antenna is a two-layer FR4 board with 0.8 mm in thickness and 10 cm in diameter. The top layer of the circuit system board is a complete conductor plane without any wires or components, which functions as the ground layer of the antenna. The bottom layer is arranged for placing components. The two boards are fixed by four 9-cm nylon columns. The input port of the rectifier and the output port of the PLL are connected to the antenna through two coaxial cables.

### B. Test of the Temperature Sensor

To evaluate the sensor's resolution, the temperature coefficients of frequency (TCF) of the output signal from the sensor

Authorized licensed use limited to: Soochow University. Downloaded on October 13,2026 at 13:10:41 UTC from IEEE Xplore. Restrictions apply.

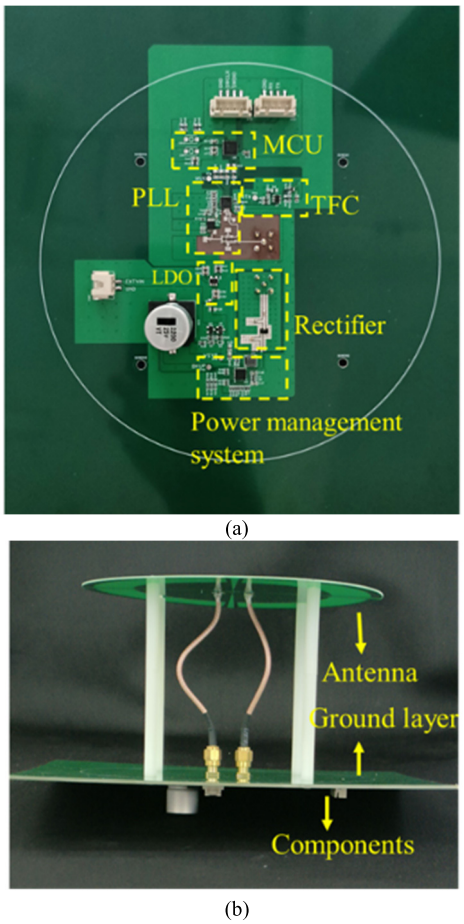



Fig. 5. Photograph of the fabricated sensing system. (a) PCB layout of the wireless temperature sensing system. (b) Fabricated dual-polarized antenna.

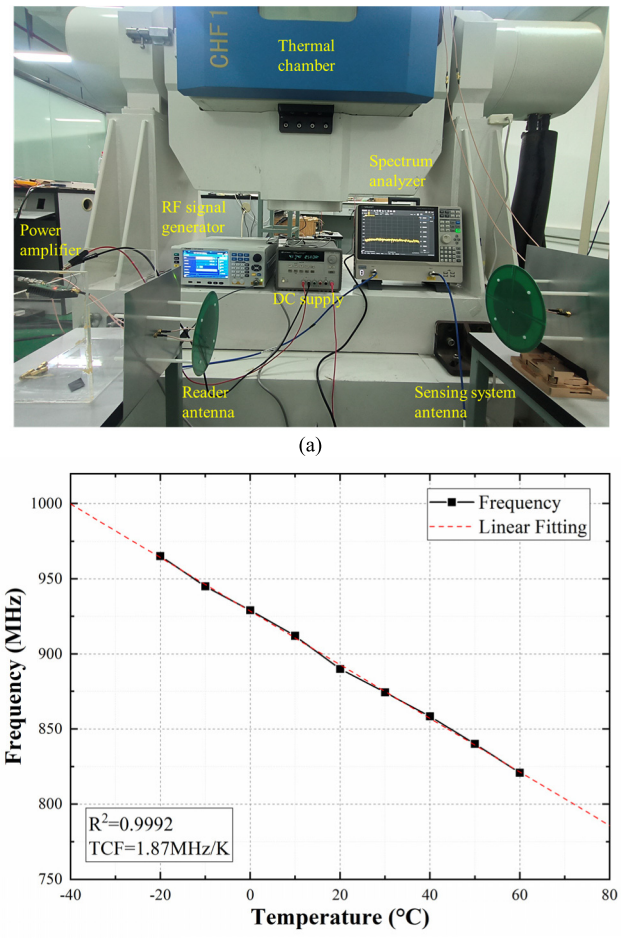



Fig. 6. Measurement environment and measured results. (a) Measurement environment. (b) Measured output frequency versus temperature curve and its linear fitting.

part and its Allan deviation $\sigma$ were measured. The resolution $S$ of the sensor is determined by the following equation:

$$S = \frac{\sigma}{\text{TCF}}. \tag{4}$$

As illustrated in Fig. 6(a), in the sensitivity test, an RF signal generator (Ceyear 1435F) was utilized to generate a signal with a power of 33 dBm and at a frequency of 997 MHz as a power source of the system. The sensing system was placed in a thermal chamber, and a spectrum analyzer (Siglent SNA5052x) measured the output frequency of the system. As constrained by experimental conditions, the tested temperature range is from −20 °C to 60 °C. Test results in Fig. 6(b) indicate a TCF of 1.83 MHz/K. The linear fitting frequency–temperature curve predicts an output frequency of 1 GHz @ −40 °C and 780 MHz @ 80 °C. Given that the VCO in the PLL has a maximum frequency of 990 MHz at −40 °C and a minimum of 770 MHz at 80 °C. The operating temperature range of the sensor is approximately −35 °C to 80 °C.

For Allan deviation characterization, the sensor part was directly powered by an external dc power supply to make the sample intervals consistent. The sensor was maintained at ambient temperature (∼26 °C), while its output frequency was continuously monitored using a spectrum analyzer

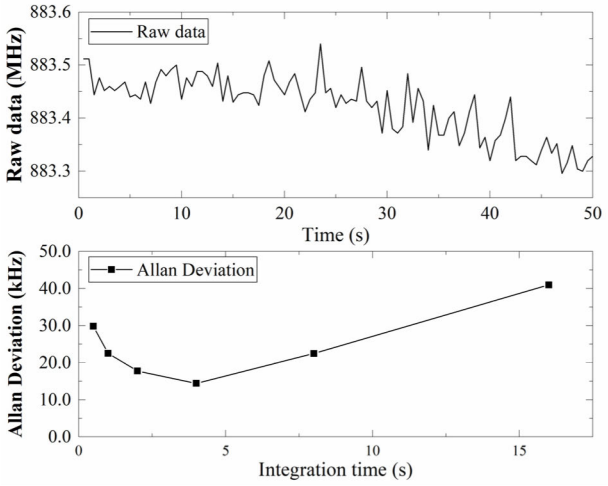



Fig. 7. Measured raw output data of the temperature sensor and calculated Allan deviation.

(Keysight N9020A). Measurements were recorded at 500-ms intervals over a 50-s duration. Fig. 7 plots the recorded raw data and the calculated Allan variance curve. The Allan deviation reaches the minimum value of 14.4 kHz when

Authorized licensed use limited to: Soochow University. Downloaded on October 13,2026 at 13:10:41 UTC from IEEE Xplore. Restrictions apply.

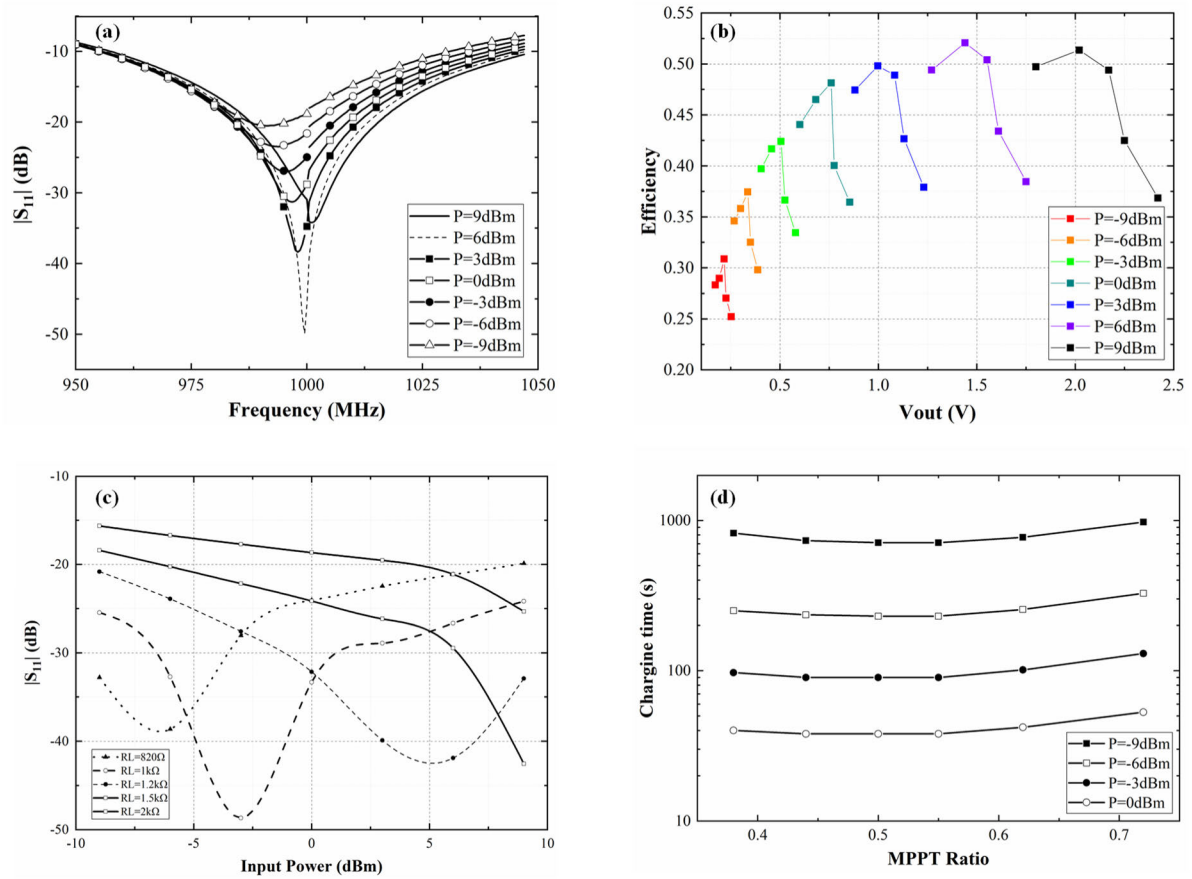



Fig. 8. (a) Measured $|S_{11}|$ of the rectifier. (b) Measured efficiency of the rectifier at different input power and work points. (c) Measured minimum $|S_{11}|$ of the rectifier with a load resistance around 1.2 kΩ versus input power. (d) Measured charging time at various input power and MPPT ratios.

the integration time $\tau$ equals 4 s. Given that the measured TCF equals 1.83 MHz/K, the sensor resolution is calculated as 7.9 mK.

### C. Test of the Rectifier

The measured $|S_{11}|$ parameter of the rectifier is shown in Fig. 8(a), indicating a matched frequency of ∼997 MHz. At this frequency, $|S_{11}|$ remains below −20 dB across all tested input power levels.

To evaluate efficiency under varying loads, the output node of the rectifier was disconnected from the power management system and connected to resistors of resistance ranging from 820 Ω to 2 kΩ to set the output voltage. An RF signal generator (Ceyear 1435F) was utilized to generate a 997-MHz RF signal at power levels ranging from −9 to 9 dBm. Rectifier efficiency $\eta$ is defined as the ratio of dc output power to RF input power

$$\eta_{\text{rec}} = \frac{P_{\text{DC}}}{P_{\text{RF}}} = \frac{V_{\text{OUT}}^2}{R \cdot P_{\text{RF}}}. \tag{5}$$

Fig. 8(b) illustrates the relationship between efficiency and output voltage at different input powers. Efficiency exceeds 30% throughout the −9- to 9-dBm range, peaking at 52% when the input power is 6 dBm. For each power level, the output voltage yielding maximum efficiency is designated the maximum power point (MPP). Fig. 8(c) shows the minimum $|S_{11}|$ value of each load resistance versus input power, which indicates that the rectifier is well matched ($|S_{11}| < -10$ dBm) within the load resistance range around the optimum value 1.2 kΩ.

When charging a supercapacitor, the capacitor voltage eventually stabilizes at the rectifier's open-circuit voltage. During initial charging stages, however, the high charging current renders the capacitor electrically equivalent to a small resistive load. This causes deviation of the working point from the MPP, reducing efficiency. Thus, implementing MPPT technology is reasonable for mitigating this issue by dynamically adjusting the working point.

### D. Test of the MPPT Controller

The MPPT controller integrated in ADP5091 is a constant proportional type controller, which makes the output voltage of the rectifier maintain a constant ratio to its open-circuit voltage (MPPT ratio, MPPTR) by adjusting the operating duty cycle of the BOOST circuit. Also, a proper MPPTR prevents the output voltage and current of the rectifier from being an extremely low value, because either a low input voltage or a low input current leads to a significant energy loss in the BOOST circuit. To test the optimum MPPTR, the charging time was tested for different powers at different MPPTRs. The charging time was defined as the time for the voltage on the capacitor to rise from $V_{\text{FALL}}$ to $V_{\text{UP}}$.

Authorized licensed use limited to: Soochow University. Downloaded on October 13,2026 at 13:10:41 UTC from IEEE Xplore. Restrictions apply.

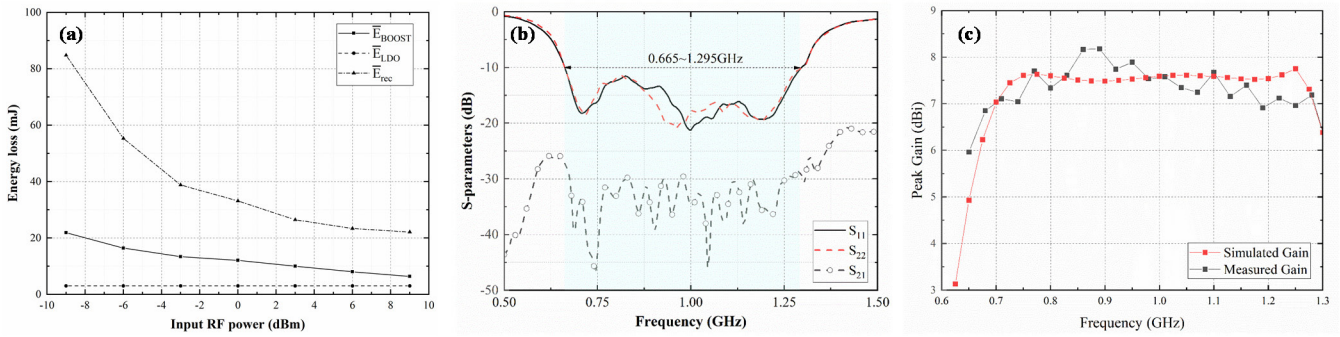



Fig. 9. (a) Contribution of circuit modules in the RF energy harvester to the total energy loss. (b) Measured $|S_{11}|$ and $|S_{21}|$ of the antenna. (c) Simulated and measured peak gain versus frequency of the antenna.

In the experiment, the storage capacitor was 2.2 mF, $V_{\mathrm{UP}}$ was set to 4.7 V, and $V_{\mathrm{FALL}}$ was set to 3.0 V. The threshold voltage has a 0.3-V difference from that mentioned above for the error of configuration resistors. Since another PCB with only energy harvester parts on it was used in this experiment. The MPPTR test focuses on operation at lower power (−9∼0 dBm), as increased efficiency under these conditions significantly reduces the charging time and facilitates an increase in the maximum operating distance. As shown in Fig. 8(d), the efficiency is maximized when the MPPTR is in the range of 0.5–0.55. Since ADP5091 has a minimum operating voltage, the MPPTR is set to 0.55 for a higher output voltage of the rectifier.

### E. Test of the Power Consumption and Loss

Each part of the RF energy harvester causes energy loss. During the charging stage, with a duration time of $\tau_{\mathrm{chr}}$, the total RF energy $E_{\mathrm{RF}}$ harvested by the RF energy harvester equals

$$E_{\mathrm{RF}} = P_{\mathrm{RF}}\tau_{\mathrm{chr}} \tag{6}$$

where $P_{\mathrm{RF}}$ refers to the power of the input RF signal. Energy loss caused by the rectifier $\bar{E}_{\mathrm{rec}}$ equals $E_{\mathrm{RF}}(1-\eta_{\mathrm{rec}})$, where $\eta_{\mathrm{rec}}$ refers to the efficiency of the rectifier.

The second stage is the BOOST circuit. The energy loss caused by the BOOST circuit $\bar{E}_{\mathrm{BOOST}}$ equals the difference between the energy stored in the capacitor during the charging stage and the total output energy of the rectifier

$$\bar{E}_{\mathrm{BOOST}} = E_{\mathrm{cap}} - E_{\mathrm{RF}}\eta_{\mathrm{rec}}. \tag{7}$$

The third stage is the LDO circuit. The energy loss caused by LDO $\bar{E}_{\mathrm{LDO}}$ is a fixed value with a dedicated threshold voltage configuration. The efficiency of LDO can be calculated through (3).

Based on the measurement results, the energy losses caused by each module and the total energy loss are estimated and plotted in Fig. 9(a). The results indicate that within the input voltage range of −9 to 9 dBm, the rectifier contributes to the predominant energy loss. At low input power levels, the overall energy conversion efficiency of the system deteriorates significantly. Therefore, increasing the antenna gain represents an effective approach to extending the operational range.

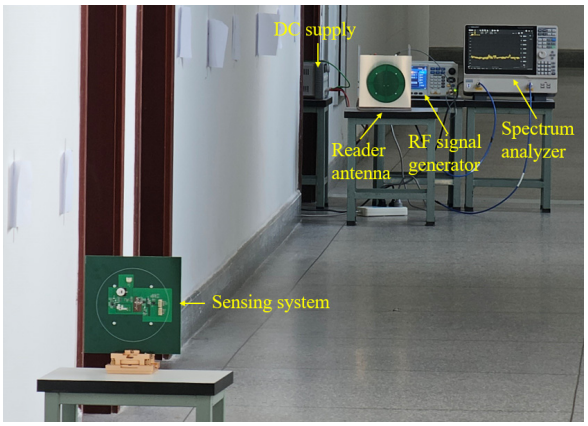



Fig. 10. Experiment of operating range.

TABLE III
DETAILED MEASURED RESULTS VERSUS DISTANCE

| Distance (m) | Charging time (s) | Received power (dBm) | Output voltage (V) |
|---|---|---|---|
| 2 | 7 | 6 | 1.38 |
| 4 | 27 | 2.8 | 1.22 |
| 6 | 87 | -2.5 | 0.6 |
| 8 | 275 | -8 | 0.38 |
| 10 | 973 | -10.5 | 0.22 |

The power consumption of the temperature sensor $P_{\mathrm{wake}}$ is measured at 60.4 mW by a multimeter. During charging, leakage current measured on the source of the MOSFET in Fig. 1 is measured at 5 nA using Agilent 33450A. During charging, the power dissipation caused by leakage current is low enough to be neglected. Therefore, the average power consumption equals

$$P_{\mathrm{avr}} = DP_{\mathrm{wake}} \tag{8}$$

where D refers to the duty cycle.

### F. Test of the Antenna

The measured S-parameters are depicted in Fig. 9(b). From the measured results, it is seen that the proposed dual-polarized antenna can obtain a wide impedance bandwidth in the frequency range of 0.665–1.295 GHz for $|S_{11}|$ less than −10 dB. Also, the isolation between the two ports is below 30 dB in the operating bandwidth, which is suitable for the wireless sensor application.

Authorized licensed use limited to: Soochow University. Downloaded on October 13,2026 at 13:10:41 UTC from IEEE Xplore. Restrictions apply.

TABLE IV
PERFORMANCE COMPARISON WITH STATE-OF-THE-ART ENERGY-HARVEST-BASED WIRELESS TEMPERATURE SENSORS

| Ref. | Energy source | Temperature range | Average power consumption | Update time | Operating distance | Resolution |
|---|---|---|---|---|---|---|
| [28] | Solar/RF | -40~180℃ | N.A. | N.A. | 27m(Solar) 7.5m(RF) | N.A. |
| [29] | EM | 0~180℃ | 3.26μW | 2.5h(60A) 6h(10A) | 70m | 0.8℃ |
| [16] | Magnetic-piezoelectric | N.A. | 59.8-966μW | 3.5min(260A) 6min(700A) | N.A. | N.A |
| [30] | N.A. | -40~180℃ | N.A. | N.A. | N.A. | 7mK |
| [31] | Thermal | RT~300℃ | N.A | N.A. | 3.4m | N.A |
| [32] | RF | 25~50℃ | 5μW | N.A. | 1.5m | 1.6℃ |
| *This work* | RF | -35~80℃ | 1.68mW(2m) 12.4μW(10m) | 7s(2m) 16min22s(10m) | 10m | 7.9mK |

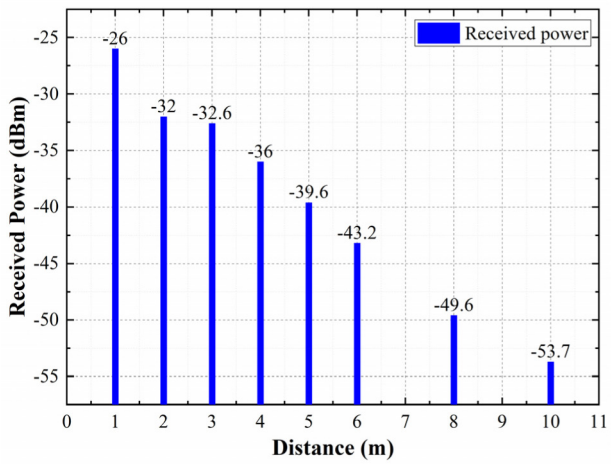



Fig. 11. Measured power of received signal at the reader versus distance.

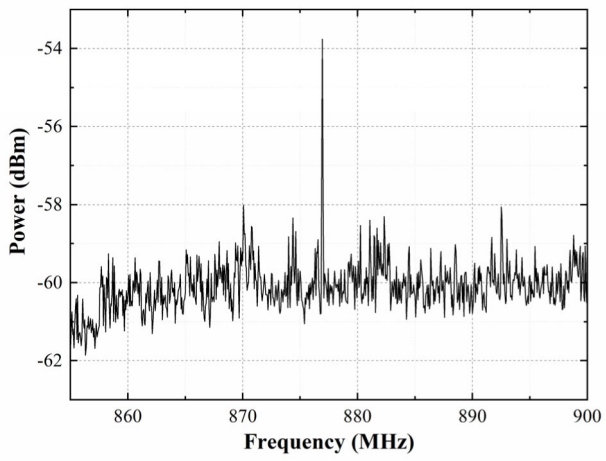



Fig. 12. Measured spectrum of the received signal at 10 m.

The simulated and measured peak gain versus frequency of the antenna around the operating frequency of the sensing system is shown in Fig. 9(c). It is seen that the peak gain at the operating frequency is ∼7 dBi. The tested gain results ensure good acceptance of the receiver in different frequency bands, which correspond to different temperatures.

## IV. SYSTEM MEASUREMENT AND RESULTS

Fig. 10 illustrates the test scenario for the operating range. The reader, comprising an RF signal generator (Ceyear 1435F), a power amplifier (PA), and a spectrum analyzer (Siglent SNA5052x), was employed to power the sensing system and detect the transmitted temperature data. During the experiment, the RF signal source and the PA were utilized to generate a signal with a power level of +33 dBm at a frequency of 997 MHz. The spectrum analyzer was used to detect the temperature signal returned from the wireless sensing system. The $V_{UP}$ voltage of the energy harvesting system was set to 4.9 V, while the $V_{FALL}$ voltage was set to 3.3 V, with a capacitor capacitance of 2.2 mF. For the test, the reader remained fixed, while the sensing system was placed at various distances. A multimeter measured the voltage across the capacitor in the sensing system to observe the charging process. The measured charging time, the power of the RF signal harvested by the system, and the output dc voltage of the rectifier versus distance are presented in Table III. The test results demonstrate that the proposed system achieves a high data update rate (<30 s) within 4 m. Also, this system is able to operate with a minimum power of −10 dBm or with a distance of 10 m to the dedicated power source, where a full charging process requires 16 min 13 s.

Fig. 11 depicts the relationship between the received signal power versus distance. At 10 m, the received signal power at the reader was measured at −53.7 dBm, confirming the system's capability of operating within a 10-m range. Fig. 12 displays the spectrum of the received signal at a 10-m distance.

According to (8), the average power consumption is calculated at 1.68 mW at a distance of 2 m and 12.4 $\mu$W at a distance of 10 m.

Finally, Table IV summarizes a comparison between the proposed wireless, energy-harvest-based sensing system and other recent works. From the comparison results, the scheme proposed in this article considers the balance of average power consumption, communication distance, and so on, under the premise of ensuring the accuracy of temperature measurement, which is very suitable for wireless high-precision temperature measurement.

## V. CONCLUSION

This article proposes an RFEH-based wireless-powered temperature sensing system comprising two main parts: a frequency-based temperature sensor and an energy harvesting circuit, as well as a dual-polarized antenna for energy and data transfer. To verify the functionality and performance of this system, tests were carried out o1.7n the temperature

Authorized licensed use limited to: Soochow University. Downloaded on October 13,2026 at 13:10:41 UTC from IEEE Xplore. Restrictions apply.

resolution, rectifier performance, MPPT performance, and antenna performance. A complete wireless self-powered sensing system was then built to carry out the wireless temperature sensing test. The experimental results demonstrate that the system can achieve a temperature resolution of 7.9 mK within the temperature range from −35 °C to 80 °C and that the energy harvesting circuit can operate at an input power of −10 dBm. The system achieves a higher temperature monitoring update rate within a range of 4 m and has a maximum working distance of around 10 m. The antenna's bandwidth meets the system's operating frequency requirements and has a gain of approximately 7 dBi within this band.

In further study, the temperature resolution can be further improved by introducing an MEMS oscillator with low phase noise and a high TCF.

## REFERENCES


[1] J. Wang et al., "Micromachined thermocouple for rapid detection of ultrahigh heat flux at high temperature," *IEEE Trans. Ind. Electron.*, vol. 69, no. 2, pp. 2099–2106, Feb. 2022, doi: 10.1109/TIE.2021.3060677.

[2] G. Zhang, G. Zhang, S. Zhu, N. Zhang, and Y. Xu, "Estimation on the hourly distribution of near-surface temperature lapse rate under winter clear-sky conditions," *IEEE Trans. Geosci. Remote Sens.*, vol. 61, 2023, Art. no. 4107013, doi: 10.1109/TGRS.2023.3327071.

[3] Y. Du, C. Zhou, Y. Feng, and L. Qiu, "Flexible, multimodal device for measurement of body temperature, core temperature, thermal conductivity and water content," *npj Flexible Electron.*, vol. 8, no. 1, Dec. 2024, doi: 10.1038/s41528-024-00373-5.

[4] K. Mahtani, J. Muñoz-Antón, S. B. Lee, and C. A. Platero, "Online diagnostics of brushless synchronous machine exciter field winding through temperature and resistance measurement," *IEEE Trans. Ind. Appl.*, vol. 61, no. 3, pp. 3774–3785, May 2025, doi: 10.1109/TIA.2025.3540983.

[5] H. Huan et al., "Real-time predictive temperature measurement in oil pipeline: Modeling and implementation on embedded wireless sensing devices," *IEEE Trans. Ind. Electron.*, vol. 68, no. 12, pp. 12689–12697, Dec. 2021, doi: 10.1109/TIE.2020.3040679.

[6] S. Javaid, H. Fahim, S. Zeadally, and B. He, "Self-powered sensors: Applications, challenges, and solutions," *IEEE Sensors J.*, vol. 23, no. 18, pp. 20483–20509, Sep. 2023, doi: 10.1109/JSEN.2023.3241947.

[7] Y. Ji, Q. Tan, H. Wang, W. Lv, H. Dong, and J. Xiong, "A novel surface *LC* wireless passive temperature sensor applied in ultra-high temperature measurement," *IEEE Sensors J.*, vol. 19, no. 1, pp. 105–112, Jan. 2019, doi: 10.1109/JSEN.2018.2872915.

[8] H. Dong et al., "Design and testing of miniaturized dual-band microstrip antenna sensor for wireless monitoring of high temperatures," *IEEE Sensors J.*, vol. 23, no. 22, pp. 27242–27250, Nov. 2023, doi: 10.1109/JSEN.2023.3315695.

[9] H. Peng, X. Yang, X. Wu, and W. Peng, "A wireless temperature sensor applied to monitor and measure the high temperature of industrial devices," *IEEE Trans. Antennas Propag.*, vol. 72, no. 6, pp. 5273–5282, Jun. 2024, doi: 10.1109/TAP.2024.3389213.

[10] C. R. Valenta and G. D. Durgin, "Harvesting wireless power: Survey of energy-harvester conversion efficiency in far-field, wireless power transfer systems," *IEEE Microw. Mag.*, vol. 15, no. 4, pp. 108–120, Jun. 2014, doi: 10.1109/MMM.2014.2309499.

[11] Q. Chen, J. Xu, W. Liu, and R. Yan, "Highly efficient power-line energy harvesting with adaptive matching capacitance for residential self-powered sensing," *IEEE Trans. Instrum. Meas.*, vol. 74, pp. 1–12, 2025, doi: 10.1109/TIM.2025.3545213.

[12] Y. Zhuang et al., "Improving current transformer-based energy extraction from AC power lines by manipulating magnetic field," *IEEE Trans. Ind. Electron.*, vol. 67, no. 11, pp. 9471–9479, Nov. 2020, doi: 10.1109/TIE.2019.2952795.

[13] A. Abasian, A. Tabesh, A. Z. Nezhad, and N. Rezaei-Hosseinabadi, "Design optimization of an energy harvesting platform for self-powered wireless devices in monitoring of AC power lines," *IEEE Trans. Power Electron.*, vol. 33, no. 12, pp. 10308–10316, Dec. 2018, doi: 10.1109/TPEL.2017.2775961.

[14] B. Andò, S. Baglio, M. Manenti, V. Marletta, A. R. Bulsara, and R. La Rosa, "Toward an autonomous sensor node exploiting a nonlinear energy harvester," *IEEE Trans. Instrum. Meas.*, vol. 73, pp. 1–10, 2024, doi: 10.1109/TIM.2024.3419138.

[15] A. Quattrocchi, F. Freni, and R. Montanini, "Power conversion efficiency of cantilever-type vibration energy harvesters based on piezoceramic films," *IEEE Trans. Instrum. Meas.*, vol. 70, pp. 1–9, 2021, doi: 10.1109/TIM.2020.3026462.

[16] P.-C. Yeh, T.-H. Chien, M.-S. Hung, C.-P. Chen, and T.-K. Chung, "Attachable magnetic-piezoelectric energy-harvester powered wireless temperature sensor nodes for monitoring of high-power electrical facilities," *IEEE Sensors J.*, vol. 21, no. 9, pp. 11140–11154, May 2021, doi: 10.1109/JSEN.2021.3056275.

[17] P. E. Araque et al., "Thermoelectric energy harvesting for oxygen determination in refrigerated intelligent packaging," *IEEE Trans. Instrum. Meas.*, vol. 69, no. 4, pp. 1353–1361, Apr. 2020, doi: 10.1109/TIM.2019.2911757.

[18] M. M. Camboim et al., "An online remote verification system of thermal sources for energy harvesting application," *IEEE Trans. Instrum. Meas.*, vol. 69, no. 10, pp. 7962–7973, Oct. 2020, doi: 10.1109/TIM.2020.2986105.

[19] G. Verma and V. Sharma, "A novel thermoelectric energy harvester for wireless sensor network application," *IEEE Trans. Ind. Electron.*, vol. 66, no. 5, pp. 3530–3538, May 2019, doi: 10.1109/TIE.2018.2863190.

[20] C. Chen et al., "Self-powered wireless sensor networks based on the radioisotope thermoelectric generator for aquatic temperature monitoring," *Appl. Thermal Eng.*, vol. 258, Jan. 2025, Art. no. 124746, doi: 10.1016/j.applthermaleng.2024.124746.

[21] Y. Fan, N. Wu, Y. Wen, and D. Zhang, "A high-efficiency self-powered wireless sensor network driven by ambient RF energy far-field," *IEEE Trans. Instrum. Meas.*, vol. 74, pp. 1–10, 2025, doi: 10.1109/TIM.2025.3552865.

[22] S. Kim et al., "Ambient RF energy-harvesting technologies for self-sustainable standalone wireless sensor platforms," *Proc. IEEE*, vol. 102, no. 11, pp. 1649–1666, Nov. 2014, doi: 10.1109/JPROC.2014.2357031.

[23] M. Aboualalaa, I. Mansour, and R. K. Pokharel, "Energy harvesting rectenna using high-gain triple-band antenna for powering Internet-of-Things (IoT) devices in a smart office," *IEEE Trans. Instrum. Meas.*, vol. 72, pp. 1–12, 2023, doi: 10.1109/TIM.2023.3238050.

[24] H. Jabbar, Young. S. Song, and T. Ted. Jeong, "RF energy harvesting system and circuits for charging of mobile devices," *IEEE Trans. Consum. Electron.*, vol. 56, no. 1, pp. 247–253, Feb. 2010, doi: 10.1109/TCE.2010.5439152.

[25] M. Gao, P. Wang, Y. Wang, and L. Yao, "Self-powered ZigBee wireless sensor nodes for railway condition monitoring," *IEEE Trans. Intell. Transp. Syst.*, vol. 19, no. 3, pp. 900–909, Mar. 2018, doi: 10.1109/TITS.2017.2709346.

[26] S.-B. Liu, F.-S. Zhang, M. Boyuan, S.-P. Gao, and Y.-X. Guo, "Multiband dual-polarized hybrid antenna with complementary beam for simultaneous RF energy harvesting and WPT," *IEEE Trans. Antennas Propag.*, vol. 70, no. 9, pp. 8485–8495, Sep. 2022, doi: 10.1109/TAP.2022.3177484.

[27] S. S. Vinnakota, R. Kumari, and B. Majumder, "Metasurface-assisted broadband compact dual-polarized dipole antenna for RF energy harvesting," *IEEE Antennas Wireless Propag. Lett.*, vol. 22, pp. 1912–1916, 2023, doi: 10.1109/LAWP.2023.3269307.

[28] A. E. Abdulhadi and R. Abhari, "Multiport UHF RFID-tag antenna for enhanced energy harvesting of self-powered wireless sensors," *IEEE Trans. Ind. Informat.*, vol. 12, no. 2, pp. 801–808, Apr. 2016, doi: 10.1109/TII.2015.2470538.

[29] M. Chen et al., "A self-powered 3.26-$\mu$W 70-m wireless temperature sensor node for power grid monitoring," *IEEE Trans. Ind. Electron.*, vol. 65, no. 11, pp. 8956–8965, Nov. 2018, doi: 10.1109/TIE.2018.2811360.

[30] S. Ji, P. Akhkandi, Y. Qi, R. Abdolvand, and H. M. Lavasani, "A wide-dynamic range (-40 °C to 180 °C) active wireless MEMS temperature sensor with 7m °C sensitivity," *IEEE Sensors J.*, vol. 23, no. 9, pp. 9194–9203, May 2023, doi: 10.1109/JSEN.2023.3262735.

[31] S. Winters et al., "High-temperature wireless sensor platform powered by energy scavenging," *IEEE Open J. Ind. Appl.*, vol. 5, pp. 63–74, 2024, doi: 10.1109/OJIA.2024.3356311.

[32] J. Wang et al., "A battery-free wireless temperature sensing chipset implemented by 55 and 65 nm CMOS process," *J. Semiconductors*, vol. 46, no. 6, Jun. 2025, Art. no. 062202, doi: 10.1088/1674-4926/25010028.


Authorized licensed use limited to: Soochow University. Downloaded on October 13,2026 at 13:10:41 UTC from IEEE Xplore. Restrictions apply.



**Zihan Yu** received the B.S. degree from Nanjing University of Information Science and Technology, Nanjing, China, in 2023. He is currently pursuing the M.S. degree in information and communication engineering with the School of Electronic and Information Engineering, Soochow University, Suzhou, China.

His research interests include front-end circuit design for micro-electromechanical (MEMS) sensors and MEMS-based temperature sensing systems.



**Changrong Liu** (Member, IEEE) received the B.E. degree in electronic information science and technology and the M.E. and Ph.D. degrees in radio physics from the University of Electronic Science and Technology of China (UESTC), Chengdu, China, in 2008, 2011, and 2015, respectively.

He is currently an Associate Professor with the School of Electronic and Information Engineering, Soochow University, Suzhou, China. His main research interests include antennas and circuits for biomedical and sensor applications.



**Baoqing Nie** received the B.S. degree from Nanjing University, Nanjing, China, in 2010, and the Ph.D. degree from the Department of Biomedical Engineering, University of California, Davis, Davis, CA, USA, in 2015.

She is currently an Associate Professor with the School of Electronic and Information Engineering, Soochow University, Suzhou, China. She has authored or co-authored more than 30 articles in refereed journals and conference proceedings. Her research interests include flexible and stretchable sensing devices and biomedical applications.



**Dacheng Xu** received the B.S. degree in physics education from Northwest Normal University, Lanzhou, China, in 1984, and the M.S. degree in circuits and systems from the University of Electronic Science and Technology, Chengdu, China, in 1992.

He was a Visiting Scholar with Twente University, Enschede, The Netherlands, and the National University of Singapore, Singapore. He is currently a Professor with the Department of Electronics and Information, Soochow University, Suzhou, China. His research interests include vibration energy harvester signal processing, MEMS inertial sensor circuit designing, and measurement technology.

Authorized licensed use limited to: Soochow University. Downloaded on October 13,2026 at 13:10:41 UTC from IEEE Xplore. Restrictions apply.